A Virion-Based Combination Vaccine Protects against Influenza and SARS-CoV-2 Disease in Mice

Ryan R. Chaparian,[a] Alfred T. Harding,[a] Cait E. Hamele,[a] Kristina Riebe,[b] Amelia Karlsson,[b] Gregory D. Sempowski,[b] Nicholas S. Heaton,[a,b] Brook E. Heaton[a]

[a]Department of Molecular Genetics and Microbiology, Duke University School of Medicine, Durham, North Carolina, USA
[b]Duke Human Vaccine Institute, Duke University School of Medicine, Durham, North Carolina, USA

Ryan R. Chaparian and Alfred T. Harding contributed equally to this article. Author order was determined based on the number of experiments completed for the article.

ABSTRACT Vaccines targeting SARS-CoV-2 have been shown to be highly effective; however, the breadth against emerging variants and the longevity of protection remains unclear. Postimmunization boosting has been shown to be beneficial for disease protection, and as new variants continue to emerge, periodic (and perhaps annual) vaccination will likely be recommended. New seasonal influenza virus vaccines currently need to be developed every year due to continual antigenic drift, an undertaking made possible by a robust global vaccine production and distribution infrastructure. To create a seasonal combination vaccine targeting both influenza viruses and SARS-CoV-2 that is also amenable to frequent reformulation, we have developed an influenza A virus (IAV) genetic platform that allows the incorporation of an immunogenic domain of the SARS-CoV-2 spike (S) protein onto IAV particles. Vaccination with this combination vaccine elicited neutralizing antibodies and provided protection from lethal challenge with both pathogens in mice. This approach may allow the leveraging of established influenza vaccine infrastructure to generate a cost-effective and scalable seasonal vaccine solution for both influenza and coronaviruses.

IMPORTANCE The rapid emergence of SARS-CoV-2 variants since the onset of the pandemic has highlighted the need for both periodic vaccination "boosts" and a platform that can be rapidly reformulated to manufacture new vaccines. In this work, we report an approach that can utilize current influenza vaccine manufacturing infrastructure to generate combination vaccines capable of protecting from both influenza virus- and SARS-CoV-2-induced disease. The production of a combined influenza/SARS-CoV-2 vaccine may represent a practical solution to boost immunity to these important respiratory viruses without the increased cost and administration burden of multiple independent vaccines.

KEYWORDS SARS-CoV-2, influenza vaccines

Every year, influenza virus vaccines are produced, distributed, and administered in numbers that are sufficient for most of the global population (1). These vaccines are widely accepted to be safe and efficacious; however, they must be reformatted annually due to viral antigenic drift (2–4). Several types of influenza vaccines are in clinical use, including purified subunit, inactivated, and live-attenuated influenza vaccines (LAIV) (1). FDA-approved subunit vaccines consist of a recombinantly expressed hemagglutinin (HA) protein, and like all current vaccination strategies, are primarily designed to elicit virus-neutralizing antibodies (5). Inactivated influenza vaccines consist of chemically inactivated viruses, are replication-incompetent, and represent the most common formulation for vaccination against influenza. In contrast, LAIVs are replication competent but are built on cold-adapted backbones which possess several mutations that limit viral replication above 33°C, thereby preventing infection of the

lower respiratory tract. LAIVs are also thought to mediate superior stimulation of CD4$^+$/CD8$^+$ T cells and uniquely elicit IgA antibodies compared to traditional inactivated influenza vaccines (6–9). Thus, a number of effective approaches have been developed to induce influenza-directed immunity.

Because of their broad use and immunogenicity, influenza viruses have also been considered as a vaccine platform. Reverse genetic approaches (10) have allowed for the introduction of noninfluenza proteins and immune epitopes into influenza viral strains (11–14). These recombinant influenza strains would then theoretically serve as vehicles for introducing these non-influenza virus antigens to the immune system. Thus, leveraging existing influenza virus vaccine production infrastructure to produce recombinant viral strains that express immunogenic antigens from other pathogens may be a practical approach to generating cost-effective, easily implemented combination vaccines or boosters.

SARS-CoV-2 is the respiratory RNA virus that causes COVID-19, a disease that is similar in many respects to influenza virus-induced disease (15). While a number of vaccines designed to vaccinate immunologically naive people and provide protection from COVID-19 are currently in use, these vaccines are for the most part expensive, associated with more significant side effects, and difficult to produce/distribute (16–19). Further complicating vaccination efforts is the emergence of mutant strains of SARS-CoV-2, such as the Delta and Omicron variants, that have been associated with reduced vaccine efficacy (20–22). Additionally, protective immunity against human coronaviruses in general is thought to be relatively short-lived (23–26). Thus, it is likely that a cost-effective, scalable, and safe vaccine to periodically boost immunity against SARS-CoV-2 will be needed.

In order to develop a platform-based solution to regularly boost immunity against SARS-CoV-2 and associated variants, we have developed and tested a combination influenza virus-based vaccine that incorporates both influenza A virus (IAV) and SARS-CoV-2 antigens. This vaccine elicited neutralizing antibodies and provided protection from lethal challenge with both viruses in mouse models of infection. By developing a vaccine strain of IAV that encodes, stably expresses, and packages a small but immunogenic domain of the SARS-CoV-2 S protein, we have generated a combination vaccine that can be manufactured in the same way that most influenza virus vaccines are already produced. To limit cost and the human vaccine burden, a seasonal IAV/SARS-CoV-2 combination vaccine could be used to replace the standard seasonal IAV vaccine and provide protection against novel variants of IAV and SARS-CoV-2. Such an approach would not require additional vaccine manufacturing or distribution facilities, and the resulting effect would be the simultaneous boosting of immunity to two respiratory pathogens.

RESULTS

Generation of an H1N1 IAV encoding the SARS-CoV-2 RBD. Our initial goal was to develop a strain of IAV that would encode a gene for the receptor binding domain (RBD) of the major antigen of SARS-CoV-2, the spike (S) glycoprotein (27, 28). We wanted this gene to be expressed at high levels and for the translated SARS-CoV-2 antigen to be incorporated into an IAV particle such that the resulting vaccine could be administered as either live attenuated or inactivated vaccine, formulations both currently approved for use in humans (29). We have previously published viral genetic approaches that allow for the incorporation of foreign open reading frames (ORFs) into the viral genome, with smaller insertions generally being better tolerated than larger ones (30–32). Using the mouse-adapted A/Puerto Rico/8/1934 (PR8) H1N1 IAV, a strain that is generally considered to be incapable of causing disease in humans (33) as the genetic background, we inserted the S RBD domain (<18% of the full-length S protein but still a complete antigenic domain) 5′ to the viral hemagglutinin (HA) ORF (Fig. 1A). This approach and genetic locus in IAV is associated with high expression of a foreign gene (30). To facilitate incorporation of the SARS-CoV-2 RBD onto nascent viral
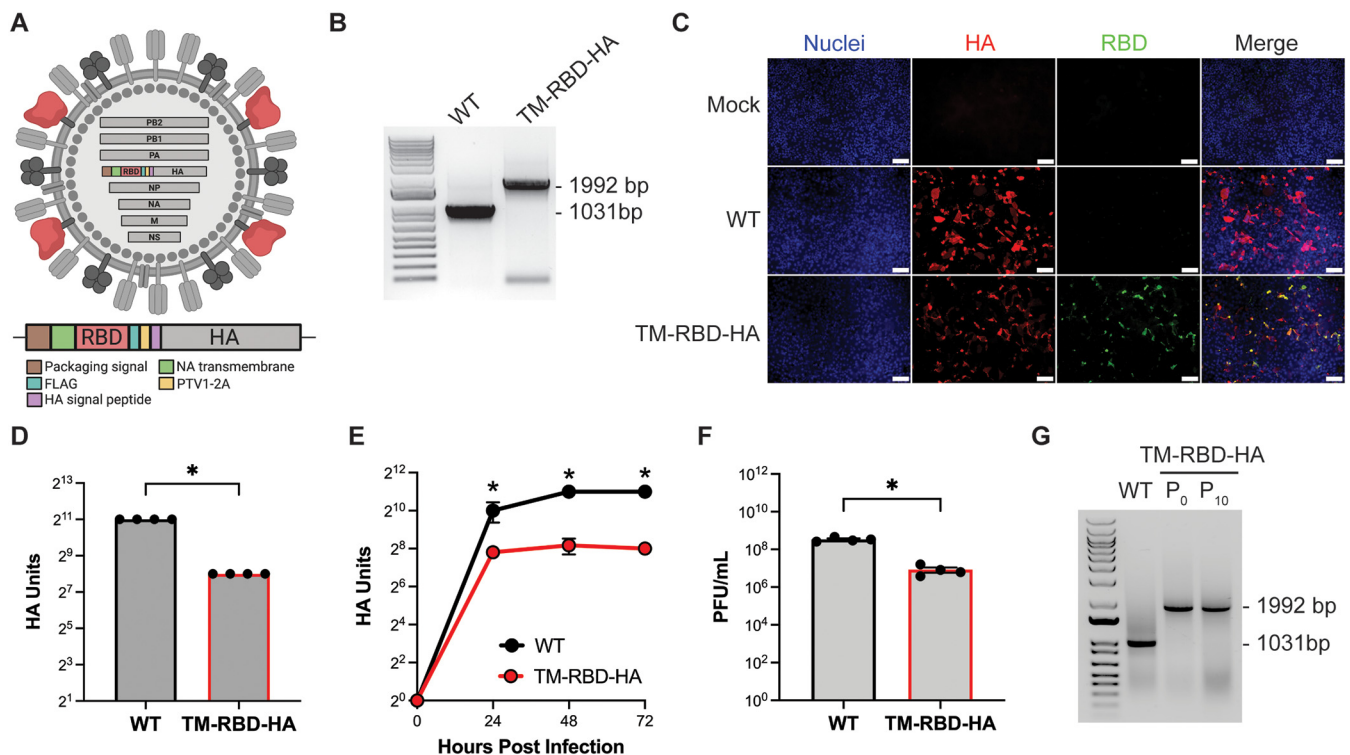
FIG 1 Generation of an IAV that encodes a vaccine antigen in the HA segment. (A) Diagram showing genetic modulation of the HA segment to enable insertion of a foreign ORF. The SARS-CoV-2 RBD was fused to the NA transmembrane domain, and a PTV1-2A site was introduced to allow for cotranslation of the RBD and HA. (B) Agarose gel showing segment 4 RT-PCRs from WT and TM-RBD-HA viruses. (C) Immunofluorescence microscopy images of unpermeabilized MDCK cells infected without virus (top), WT virus (middle), or TM-RBD-HA virus (bottom); cells were subsequently stained with antibodies/dyes against nuclei (first column), HA (second column), or SARS-CoV-2 RBD (third column). Merged images are presented in the fourth column. Scale bar indicates 100 μm. (D) HA assays of WT and TM-RBD-HA viruses after growth in embryonated chicken eggs for 72 h. Each dot represents an individual egg; $n = 4$. (E) HA assays of WT and TM-RBD-HA viruses grown in embryonated chicken eggs at 24, 48, and 72 h; $n = 4$. (F) Plaque assays of WT and TM-RBD-HA viruses after growth in embryonated chicken eggs for 72 h from panel E. Each dot represents an individual egg; $n = 4$. (G) Segment 4 RT-PCRs with WT and TM-RBD-HA viruses after 10 passages on MDCK cells. P0 indicates the stock of virus used for the experiment. Statistical analyses were performed using unpaired Mann-Whitney tests. For all panels, asterisks indicate P values of <0.05. Error bars indicate the standard error of the mean (SEM).

particles, we fused the ORF to the N-terminal sequence from the IAV neuraminidase (NA) protein which contains the transmembrane domain and cytoplasmic tail of that protein. In between the two proteins is a picornaviral 2A motif which ensures that the proteins are cotranslationally separated and can be independently packaged onto the viral particle (Fig. 1A).

We rescued the virus and verified appropriate insertion of the SARS-CoV-2 RBD ORF into the HA-encoding IAV segment via reverse transcriptase PCR (RT-PCR) (Fig. 1B). To determine if the RBD was being expressed and localized to the plasma membrane, we infected cells, fixed them (but did not permeabilize), and then incubated them with antibodies against the IAV HA protein and the SARS-CoV-2 RBD. While infection with both non-modified wild-type (WT) IAV as well as the recombinant vaccine strain (TM-RBD-HA) led to expression of HA, the SARS-CoV-2 RBD was only detectable after infection with the TM-RBD-HA virus (Fig. 1C). In multicycle growth assays, the TM-RBD-HA virus amplified itself, although with delayed kinetics and a lower endpoint titer compared to WT PR8 (Fig. 1D to F). Finally, we wanted to ensure that the SARS-CoV-2 RBD ORF would remain stable in the viral genome. After 10 serial passages, the SARS-CoV-2 RBD ORF was amplified via RT-PCR with no apparent changes to its size (Fig. 1G). DNA sequencing of this RT-PCR product revealed no mutations in the SARS-CoV-2 RBD or flanking genetic elements. Thus, we successfully developed an IAV vaccine that incorporates a membrane-anchored SARS-CoV-2 RBD antigenic domain.

The SARS-CoV-2 RBD is packaged onto IAV particles without disruption of native viral proteins. Next, we wanted to ensure that the membrane-anchored SARS-CoV-2 RBD was, in fact, incorporated into the viral particle. We therefore purified WT
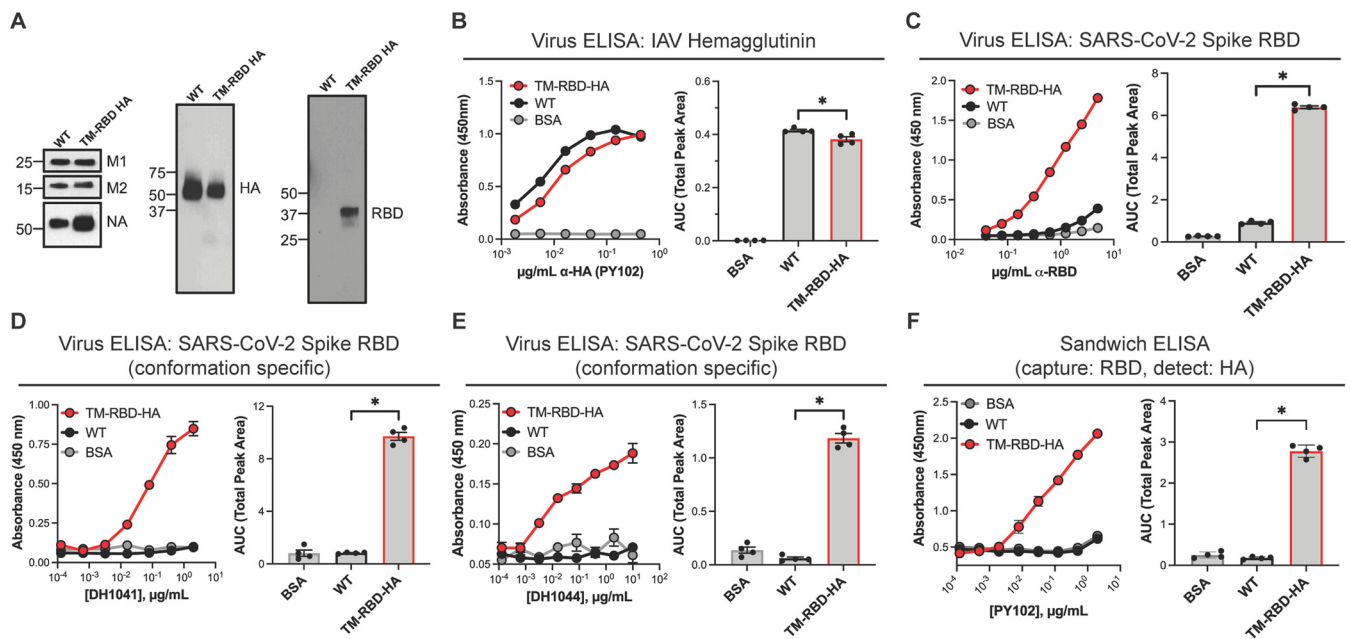
FIG 2 The SARS-CoV-2 RBD is stably incorporated into IAV particles without disrupting other viral envelope proteins. (A) Western blot analysis of WT and TM-RBD HA viral particles purified after growth in embryonated chicken eggs. Samples were normalized via M1 protein signal using pixel densitometry. (B) ELISAs (left) against whole virus particles using the PY102 anti-HA antibody and area under the curve analysis (right, $n = 4$). (C) ELISAs (left) against whole virus particles using a SARS-CoV-2 RBD antibody (binds a nonstructural epitope) and area under the curve analysis (right, $n = 4$). (D) ELISAs (left) against whole virus particles using a SARS-CoV-2 neutralizing antibody (DH1041, binds a structural epitope on the RBD) and area under the curve analysis (right, $n = 4$). (E) Same analysis as in panel D using a different conformation-specific SARS-CoV-2 neutralizing antibody, DH1044 ($n = 4$). (F) Sandwich ELISA of WT/TM-RBD-HA viruses in which DH1041 antibody was used to capture virus and PY102 was subsequently used to detect virus; $n = 4$. Statistical analyses were performed using unpaired Mann-Whitney tests. For all panels, asterisks indicate P values of <0.05. Error bars indicate the SEM.

and TM-RBD-HA virus particles and analyzed their protein composition via Western blot analysis. We first normalized loading based on the levels of the IAV matrix (M1) protein in the two samples; the M1 protein forms the viral capsid and is not expected to be altered by changes to glycoprotein composition (34). As expected, we observed that SARS-CoV-2 RBD was detectable in the recombinant RBD virus, but not in the WT virus (Fig. 2A). To determine the influence of the incorporation of another protein in the viral envelope on the native influenza viral surface proteins, we probed for expression of M2 as well as the HA and NA proteins. While the levels of the M2 protein were unchanged, there was a slight reduction in the amount of HA and an increase in the amount of NA packaged into nascent virions compared to WT virus (Fig. 2A). Thus, this genetic approach can facilitate packaging of a foreign protein onto a viral particle without dramatic effects on native viral protein incorporation.

We next wanted to assess native glycoprotein virion packaging and the SARS-CoV-2 RBD secondary structure on intact virions. Via enzyme-linked immunosorbent assay (ELISA) on purified virions, we observed a statistically significant but minor reduction of HA in the recombinant TM-RBD-HA virus compared to unmodified WT virus (Fig. 2B). We then probed for the SARS-CoV-2 RBD using antibodies that recognize either nonstructural or structural epitopes. A nonconformation-specific antibody raised against the RBD yielded strong signal only against the RBD virus (Fig. 2C). To verify that the TM-RBD fusion protein was folding correctly, we utilized DH1041 and DH1044, which are conformation-specific human monoclonal antibodies that bind the SARS-CoV-2 RBD (35, 36). Both antibodies specifically bound the TM-RBD-HA virus and not the parental WT IAV (Fig. 2D and E). In order to confirm that the RBD and HA proteins were packaged together into the same viral particles, we performed sandwich ELISAs. As expected, only the TM-RBD-HA samples had significant signal, indicating that virions harboring the RBD also possessed HA (Fig. 2F). Taken together, these results indicate that the recombinant TM-RBD-HA virus packages properly folded SARS-CoV-2 RBD

protein while maintaining the packaging of the other IAV envelope proteins HA, NA, M1, and M2.

The TM-RBD-HA virus is attenuated *in vitro*/*in vivo* and does not functionally bind ACE2. Our IAV-based vaccine virus incorporated a small antigenic domain of the SARS-CoV-2 S protein, which was not expected to confer any biologically relevant functionality. To ensure this was the case, we first performed a multicycle growth curve analysis on A549 cells harboring or lacking the SARS-CoV-2 receptor protein, ACE2. In both experiments, the TM-RBD-HA virus had lower endpoint titers and reduced replication kinetics of similar magnitudes compared to WT virus (Fig. 3A). Next, we generated a panel of pseudotyped lentiviral vectors that express luciferase after successful cellular entry; these vectors allowed us to test the ability of the TM-RBD protein to mediate infection by itself. While both vesicular stomatitis virus G (VSV-G) and the IAV HA and NA glycoproteins were sufficient to allow viral entry, the TM-RBD protein alone was insufficient to transduce either A549 or A549-*ACE2* cells (Fig. 3B). In fact, the addition of the TM-RBD with the HA and NA significantly reduced the ability of the pseudotyped virus to transduce both cell lines, indicating that TM-RBD-mediated alterations to native HA/NA glycoprotein packaging may potentially be a driver of the attenuation observed with our vaccine virus.

Next, to ensure that the entry of our vaccine virus was completely dependent on the canonical IAV HA-sialic acid interaction (37), we infected A549-*ACE2* cells after treatment with Sialidase A, a technique which removes sialic acids from cell surface glycoproteins. For both the WT IAV and the TM-RBD-HA virus, treatment with Sialidase A decreased the infection rate by the same extent and to nearly the limit of detection (Fig. 3C and D). We also compared the neutralizing potency of PY102, an HA-targeting monoclonal antibody, against WT and TM-RBD-HA viruses using plaque reduction neutralization tests (PRNTs). The $PRNT_{50}$ of PY102 was unchanged when used against both the WT and TM-RBD-HA viruses (Fig. 3E). Finally, to ensure that our *in vitro* observations would be consistent with viral phenotypes *in vivo*, we infected K18-*hACE2* mice, which express hACE2, the human SARS-CoV-2 receptor, and support SARS-CoV-2 infection (38), with multiple doses of both WT and TM-RBD-HA IAV. For all viral inoculums, murine morbidity and mortality were significantly reduced for the TM-RBD-HA virus compared to the WT virus (Fig. 3F, G). Thus, the presence of the TM-RBD on the vaccine virus particle conferred no measurable benefit to the entry of the virus; in fact, attenuation and modest inhibition of entry specifically could be measured in our assays.

Inactivated TM-RBD-HA vaccination provides incomplete immunity against IAV and SARS-CoV-2. Our next step was to define the immune responses after vaccination with the TM-RBD-HA virus. First, we prepared inactivated whole-virion vaccines by treating virus with formalin. Although standard inactivated influenza vaccines are typically "split-inactivated" by detergent treatment, the immunogenicity of formalin-inactivated influenza vaccines has been shown to induce similar responses (39). We performed an inactivated prime-boost regimen followed by serum IgG characterization or challenge with a lethal dose of IAV or SARS-CoV-2 (Fig. 4A). Analysis of immune sera from both vaccinated groups revealed that high levels of anti-HA antibodies were elicited by both vaccines, and antibody levels were increased after the boost (Fig. 4B). These IAV-directed antibodies neutralized PR8 *in vitro*; however, sera from WT-vaccinated animals neutralized more efficiently (Fig. 4C). Despite the differences in the neutralizing capacity of the sera, both vaccinations protected mice after challenge with 10 times the 50% lethal dose (LD_{50}) of PR8, likely by reducing the viral burden and the pathological effects of IAV infection (Fig. 4D to G). SARS-CoV-2 RBD-reactive serum IgG antibodies were detectable specifically in mice vaccinated with the TM-RBD-HA virus, as expected; however, the titers were insufficient to neutralize infectious SARS-CoV-2 virus (Fig. 4H and I). Consistent with the *in vitro* data, the inactivated TM-RBD-HA vaccine was not able to protect against lethal challenge with SARS-CoV-2 in this model and showed comparable viral burden in the lungs of mice as well as histological effects of infection (Fig. 4J to M).
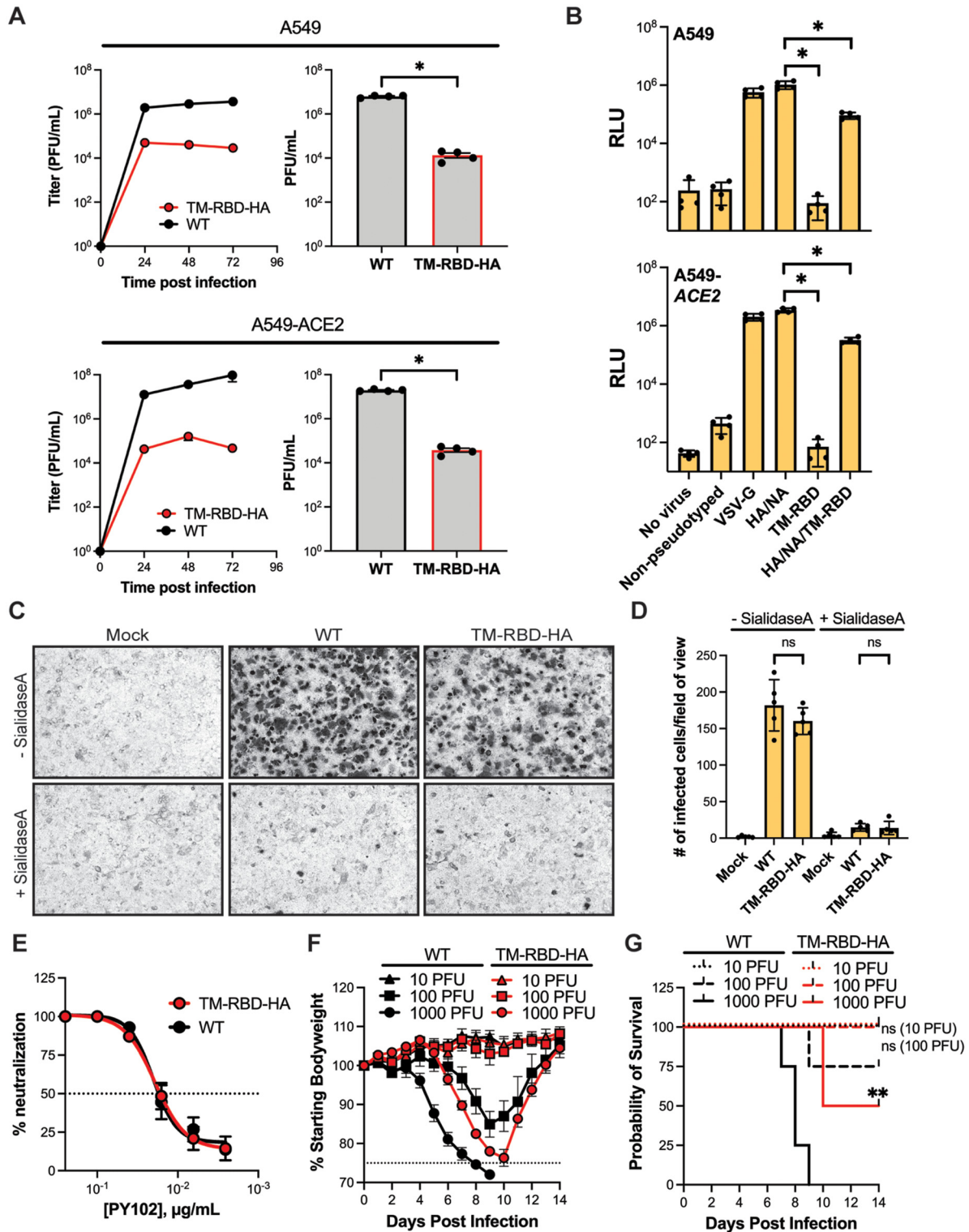
FIG 3 The TM-RBD-HA virus is attenuated *in vitro* and *in vivo* and does not functionally bind ACE2. (A) Growth curves ($n = 3$) and endpoint titers ($n = 4$) of WT and TM-RBD-HA viruses on A549 and A549-*ACE2* cells. (B) Transduction of A549 and A549-*ACE2* cells with pseudotyped lentiviral particles; relative light units (RLU) were measured as a proxy for cell entry ($n = 4$). (C) Infection of Sialidase A-treated A549-*ACE2* cells with WT and TM-RBD-HA viruses. (D) Number of infected cells from 5 representative sections from panel C. (E) PRNTs using anti-HA PY102 with WT and TM-RBD-HA viruses ($n = 4$). (F) Body weights of K18-*hACE2* mice infected with WT or TM-RBD-HA viruses ($n = 4$). (G) Survival of mice from panel F. Statistical analyses were performed using unpaired Mann-Whitney tests for panels A, B, and D and Mantel-Cox tests for panel G. For survival plots, statistical tests were applied to compare the survival rates of mice infected with the same amount of WT or TM-RBD-HA virus. For all panels, P values denoted with asterisks correspond to the following values: **, $P < 0.01$; *, $P < 0.05$; ns, not significant. Dotted lines represent PRNT$_{50}$ or humane endpoints. Error bars indicate the SEM.
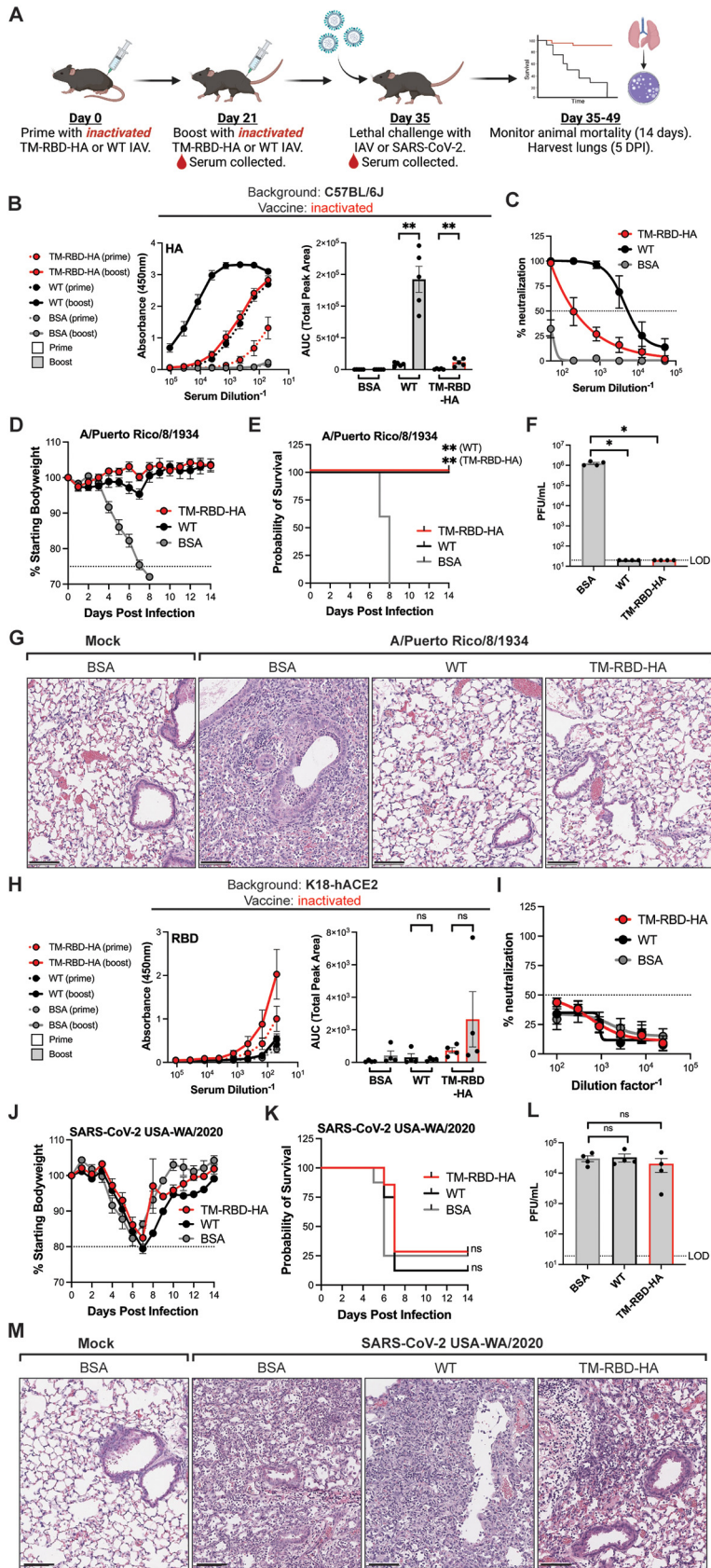
FIG 4 Vaccination of mice with inactivated TM-RBD-HA virus elicits neutralizing antibody responses and protective immunity against IAV but not SARS-CoV-2. (A) Experimental design for the inactivated

(Continued on next page)

Live-attenuated TM-RBD-HA vaccination provides improved immunity against IAV and SARS-CoV-2 relative to inactivated vaccine formulations. Live-attenuated influenza virus vaccination has been reported to provide superior protection relative to inactivated formulations in humans (40). Since our vaccine virus was naturally attenuated by addition of the RBD antigen, but failed to provide protection from SARS-CoV-2 as an inactivated formulation, we altered our vaccination strategy. We first administered an intranasal live-attenuated vaccine followed by an inactivated boost 21 days later (Fig. 5A). Influenza virus-specific HA- and neuraminidase (NA)-reactive antibodies were detected after the prime, and their levels were increased after inactivated virus boost (Fig. 5B and C). Further, direct comparison of the inactivated and live-attenuated vaccination strategies demonstrated that, indeed, a live-attenuated prime led to significantly higher-magnitude antibody responses (Fig. 5D). As with the inactivated formulation, the IAV-directed antibodies elicited by live-attenuated vaccination were also able to neutralize infectious IAV similarly to sera from WT-vaccinated mice (Fig. 5E and F). Similarly, when SARS-CoV-2 RBD-reactive antibodies were measured, we observed specific induction after TM-RBD-HA vaccination, and higher magnitude responses were elicited after the live-attenuated compared to the inactivated approach (Fig. 5G and H). Notably, PRNT analyses with live-attenuated vaccination serum showed that the postvaccination sera were able to efficiently neutralize infectious SARS-CoV-2 virus (Fig. 5I and J).

Vaccination with live TM-RBD-HA virus provides protective immunity against IAV and SARS-CoV-2. After demonstrating the presence of serum neutralizing antibodies against both IAV and SARS-CoV-2, we next sought to determine if these responses would be sufficient to provide protection from lethal IAV and SARS-CoV-2 challenge. C57BL/6J or K18-h*ACE2* mice were therefore primed with the live-attenuated vaccine and boosted with inactivated virus or bovine serum albumin (BSA) (Fig. 6A). The vaccinated C57BL/6J mice were then challenged with a lethal dose of A/Puerto Rico/8/1934 IAV. Animals vaccinated with either WT or TM-RBD-HA virus were protected from any detectable morbidity, and all animals survived the challenge, in contrast to the BSA control-vaccinated animals (Fig. 6B and C). Infectious IAV particles were also reduced to below the limit of detection in vaccinated mouse lung homogenates compared to more than 10^5 PFU/mL of lung homogenate in unvaccinated mice (Fig. 6D), and, as expected, histological analysis of lung tissue from mice that received either WT or TM-RBD-HA vaccines were indistinguishable from mock-infected animals (Fig. 6E).

In parallel, the live-attenuated vaccinated K18-h*ACE2* mice were challenged with a lethal dose of SARS-CoV-2. Animals vaccinated with WT virus or BSA showed rapid

FIG 4 Legend (Continued)

vaccination and challenge. (B) ELISAs (left) against purified soluble HA and area under the curve analysis (right) using sera from C57BL/6J mice vaccinated with inactivated virus ($n = 5$). (C) Plaque reduction neutralization tests (PRNT) with sera from vaccinated C57BL/6J mice against live A/Puerto Rico/8/1934 virus ($n = 5$). (D) Body weights of C57BL/6J mice vaccinated with either WT virus, TM-RBD-HA virus, or BSA and challenged with a lethal dose (500 PFU) of A/Puerto Rico/8/1934 ($n = 5$). (E) Survival of mice from panel D. (F) Quantification of IAV PFU in lung homogenates from vaccinated/challenged C57BL/6J mice ($n = 4$). (G) Lung tissue histology (hematoxylin and eosin [H&E] staining) of vaccinated/challenged C57BL/6J mice (representative images, $n = 3$). (H) ELISAs (left) against purified soluble RBD protein and area under the curve analysis (right) using sera from K18-*hACE2* mice vaccinated with inactivated virus ($n = 4$). (I) Sera from mice vaccinated with inactivated TM-RBD-HA virus ($n = 4$) were used for PRNTs against SARS-CoV-2 USA-WA/2020. (J) Body weights of K18-*hACE2* mice vaccinated with either WT, TM-RBD-HA, or BSA and challenged with a lethal dose (3×10^4 PFU) of SARS-CoV-2 USA-WA/2020 ($n = 8$, except TM-RBD-HA, $n = 7$). (K) Survival of mice from panel J. (L) Quantification of CoV PFU in lung homogenates from vaccinated/challenged K18-*hACE2* mice ($n = 4$). (M) Lung tissue histology (H&E staining) of vaccinated/challenged K18-*hACE2* mice (representative images, $n = 3$). Statistical analyses were performed using unpaired Mann-Whitney tests except for the survival analysis, which used Mantel-Cox tests. For survival plots, statistical tests were applied to compare the WT/TM-RBD-HA groups against the BSA group. For all panels, P values denoted with asterisks correspond to the following values: *, $P < 0.05$; **, $P < 0.01$; ns, not significant. For all microscopy images, the scale bar indicates 200 μm. Error bars indicate the SEM. Dotted lines represent the limit of detection (LOD), PRNT$_{50}$, or humane endpoints; for undetectable samples, data points have been assigned the LOD value.
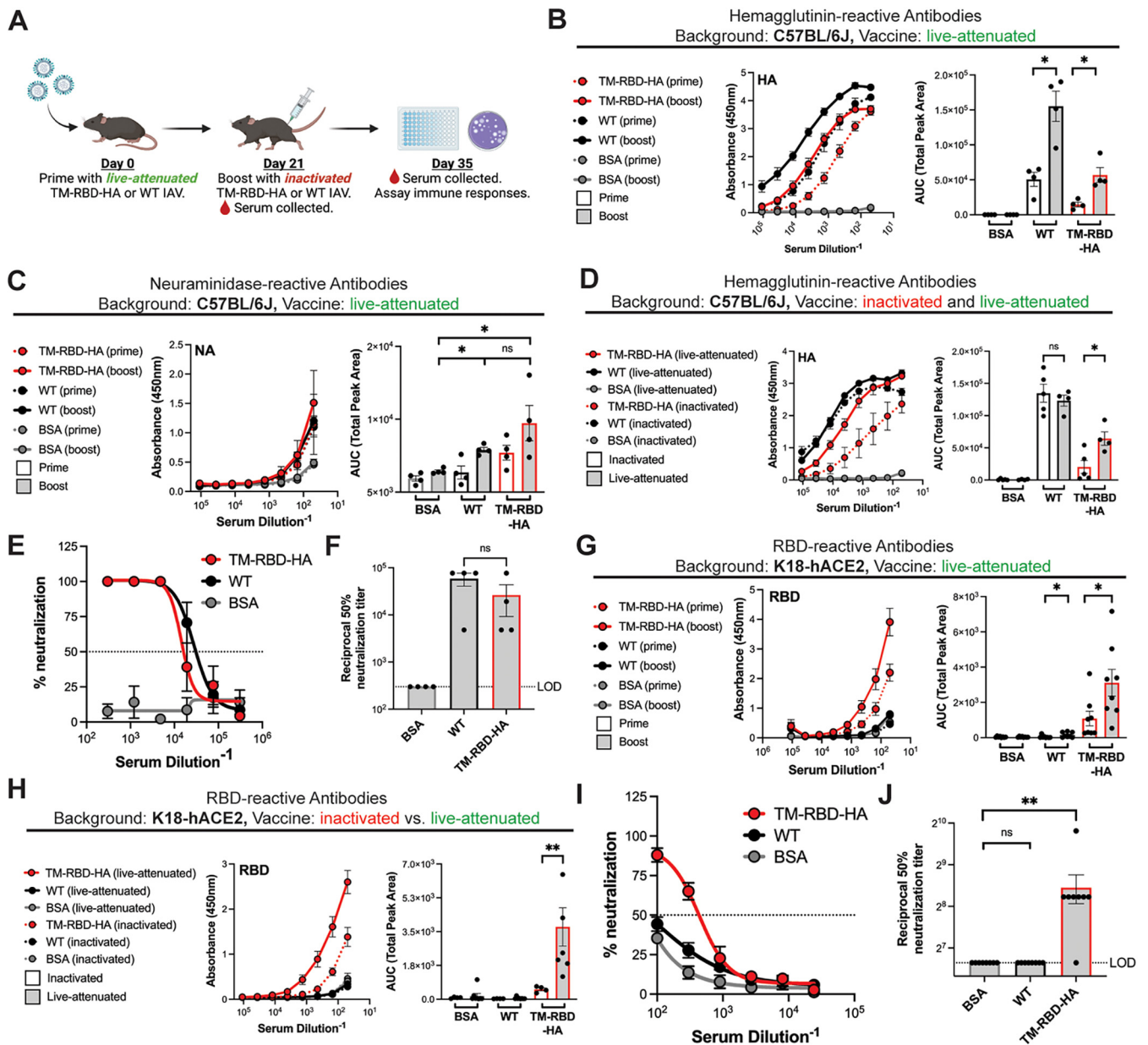
FIG 5 Live-attenuated vaccination of mice with TM-RBD-HA virus elicits neutralizing antibody responses against both IAV and SARS-CoV-2. (A) Diagram illustrating vaccination and sample collection time points. (B) (Left) ELISAs against purified soluble HA protein using sera from C57BL/6J mice vaccinated with the live-attenuated regimen ($n = 4$). (Right) Area under the curve analysis. (C) (Left) ELISAs against purified soluble NA protein using sera from C57BL/6J mice vaccinated with the live-attenuated regimen ($n = 4$). (Right) Area under the curve analysis. (D) ELISAs (left) against purified soluble HA protein and area under the curve analysis (right) using sera from C57BL/6J mice vaccinated with either the live-attenuated regimen ($n = 4$) or the inactivated regimen ($n = 5$). (E) PRNTs with sera from vaccinated C57BL/6J mice against live A/Puerto Rico/8/1934 virus ($n = 4$). (F) Neutralization titer quantification of PRNTs from panel E. (G) ELISAs against purified soluble RBD protein using sera from K18-*hACE2* mice vaccinated with the live-attenuated regimen ($n = 8$). (Right) Area under the curve analysis. (H) ELISAs (left) against purified soluble RBD protein and area under the curve analysis (right) using sera from K18-*hACE2* mice vaccinated with the live-attenuated regimen ($n = 4$) or inactivated regimen ($n = 8$ for BSA and WT $n = 7$ for TM-RBD-HA). (I) PRNTs with sera from vaccinated K18-*hACE2* mice against live SARS-CoV-2 USA-WA/2020 virus ($n = 8$). (J) Neutralization titer quantification of PRNTs from (I). Statistical analyses were performed using unpaired Mann-Whitney tests. For all panels, *P* values denoted with asterisks correspond to the following values: **, $P < 0.01$; *, $P < 0.05$; ns, not significant. Error bars indicate the SEM. Error bars corresponding to values less than 0 have been clipped from panel E. Dotted lines represent the limit of detection (LOD) or PRNT$_{50}$; for undetectable samples, data points have been assigned the LOD value.

weight loss and predominantly succumbed to the infection, while the TM-RBD-HA mice displayed no measurable weight loss, and all animals survived the challenge (Fig. 6F and G). High levels of infectious SARS-CoV-2 were also detectable in lung homogenates of WT-vaccinated animals, while the burden in TM-RBD-HA-vaccinated animals
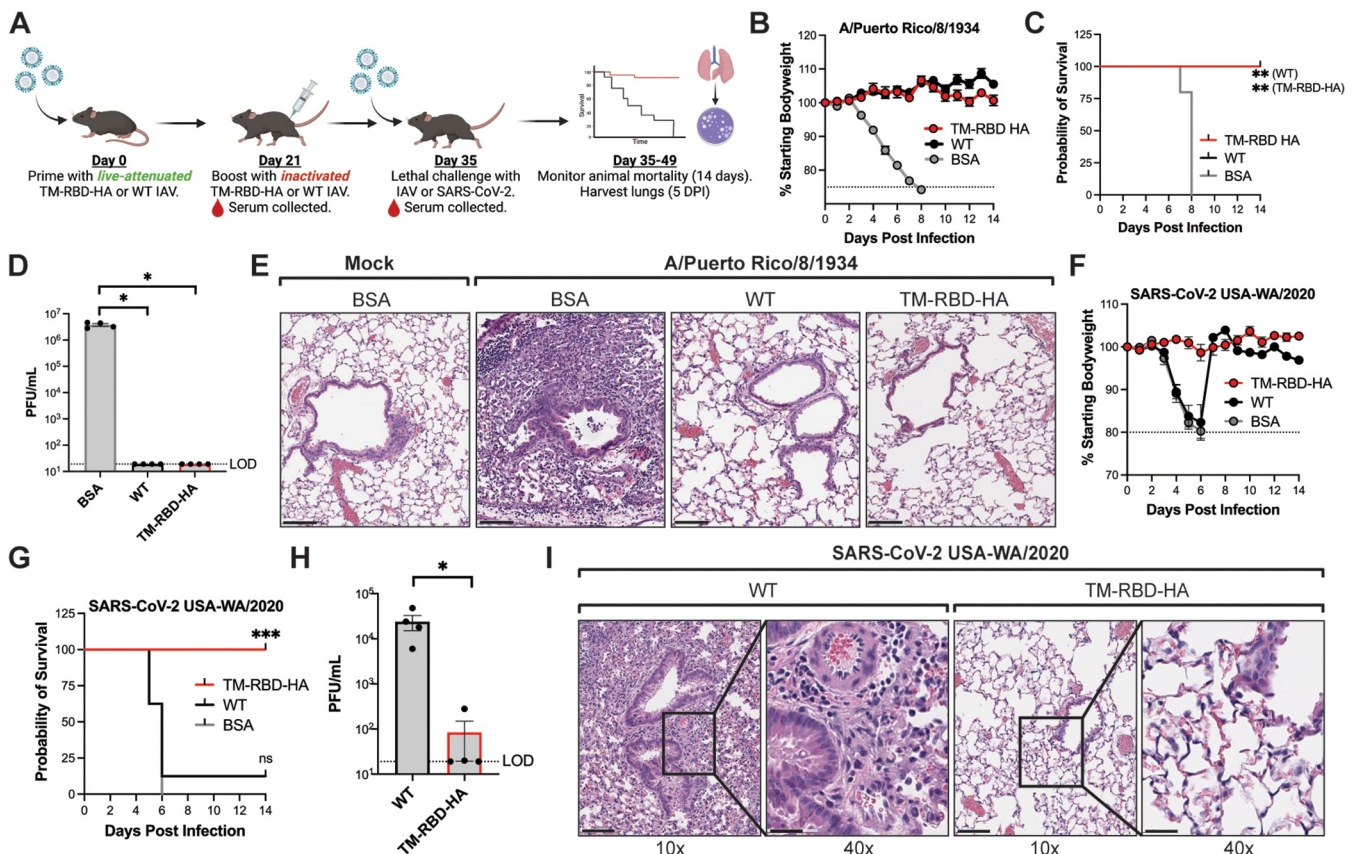
FIG 6 Live-attenuated vaccination with TM-RBD-HA virus provides protection against IAV and SARS-CoV-2 challenge in mice. (A) Experimental design displaying vaccination/challenge time points. (B) Body weights of C57BL/6J mice vaccinated with either WT virus, TM-RBD-HA virus, or BSA and challenged with a lethal dose of A/Puerto Rico/8/1934 (n = 5). (C) Survival of mice from (B). (D) Quantification of IAV PFU in lung homogenates from vaccinated/challenged mice (n = 5). (E) Lung tissue histology (H&E staining) of mice challenged with A/Puerto Rico/8/1934 (representative images, n = 3). (F) Body weights of K18-h*ACE2* mice vaccinated with either WT virus, TM-RBD-HA virus, or BSA and challenged with a lethal dose of SARS-CoV-2 USA-WA/2020, (n = 8, except TM-RBD-HA, n = 7). (G) Survival of mice from panel F. (H) Quantification of CoV PFU in lung homogenates from vaccinated/challenged mice (n = 4). (I) Lung tissue histology (H&E staining) of mice challenged with SARS-CoV-2 USA-WA/2020 (representative images, n = 4). For all microscopy images, the scale bars indicate 200 μm and 50 μm for the ×10 and ×40 magnified samples, respectively. Unpaired Mann-Whitney tests and Mantel-Cox tests were used for panels D/H and C/G, respectively. For survival plots, statistical tests were applied to compare WT/TM-RBD-HA groups against the BSA group. For all panels, P values denoted with asterisks correspond to the following values: ***, $P < 0.001$; **, $P < 0.01$; *, $P < 0.05$. Error bars indicate the SEM. Dotted lines represent the limit of detection (LOD) or humane endpoints; for undetectable samples, data points have been assigned the LOD value.

was significantly reduced (Fig. 6H). Lung tissue morphology was also investigated after challenge with SARS-CoV-2, and mice that received WT vaccine harbored severe lung infiltration/inflammation compared to mice that received TM-RBD-HA vaccine (Fig. 6I). Taken together, these data demonstrate that a live-attenuated vaccination with our combination TM-RBD-HA yields strong protective immunity against both IAV and SARS-CoV-2.

DISCUSSION

In general, the development and production of novel vaccines is labor-intensive, costly, and difficult to scale upon high demand. There are many different influenza vaccines used worldwide, including split-inactivated, live-attenuated, and recombinant protein-based vaccines. The existing infrastructure for producing influenza vaccines is highly optimized and capable of delivering more than a billion doses per year (41). In order to potentially leverage the influenza vaccine infrastructure for the production of other vaccines, we have demonstrated that a laboratory-adapted IAV vaccine backbone (A/Puerto Rico/8/1934) can be used to express and package the RBD from the spike protein of SARS-CoV-2. Vaccination of naive mice with this vaccine virus administered as a live-attenuated vaccine followed by an inactivated boost elicited neutralizing antibodies and protected against lethal challenge from both IAV and SARS-CoV-2.

Thus, an influenza virus-based vaccine platform may be a practical solution for the production of a combination seasonal vaccine produced in an analogous manner to standard influenza vaccines.

Our data are in general agreement with previous work that has shown influenza viruses can be used as a vector to express other antigens. From expressing additional influenza proteins (30, 42, 43) to expression of antigens and/or epitopes for pathogens as divergent as *Mycobacterium tuberculosis* (44) and *Chlamydia trachomatis* (45), the IAV can be modified to help elicit noninfluenza directed responses from the immune system. In fact, prior to this study, encoding the SARS-CoV-2 RBD gene into the influenza virus genome has been described. Loes et al. successfully generated a live-attenuated ΔNA(RBD) virus which packages the SARS-CoV-2 RBD but lacks NA and requires a mutation in the HA coding sequence to reduce affinity to sialic acid; vaccination with this virus was able to induce neutralizing SARS-CoV-2 antibodies (46). Another combination SARS-CoV-2/influenza live-attenuated virus vaccine has even advanced into human clinical trials (47, 48). Our approach has different strengths compared to these studies, including the ability to package the noninfluenza antigen onto viral particles rather than restricted expression of the antigen in infected cells. Irrespective of the specifics of the vaccine design, however, it is clear that influenza virus-based vaccines, delivered either as live-attenuated or inactivated formulations, can elicit protection against other pathogens.

There also remain a number of questions to be answered in future studies. Perhaps the most obvious question is the magnitude of protection provided by vaccination with the RBD domain alone compared to the full S protein. Much SARS-CoV-2 vaccine work has focused on full-length S protein, including live, virally vectored vaccines. In addition to adenovirus vectors, Newcastle disease virus (NDV) and measles viruses harboring the spike protein have been shown to induce strong protection (49–52). While our data show that vaccine responses against the RBD alone in naive animals are sufficient to mediate some protection, it will be important to understand vaccination effects in models with preexisting IAV/SARS-CoV-2 immunity, as well as to determine if boosting only RBD-directed responses is ultimately an efficacious strategy in people. Another outstanding question is whether or not boosting RBD-directed immune responses will be sufficient to mediate protection against different SARS-CoV-2 variants. If so, an added benefit to including the RBD in the influenza vaccine is that most current influenza vaccines contain four influenza strains, two IAV and two IBV strains. This would allow the ability to include up to four different SARS-CoV-2 variant RBDs, or 4 times the amount of one RBD; however, both the feasibility of incorporating RBD in different HA segments and the immunity cost of incorporating the RBD into the HA segment of another influenza virus are yet to be experimentally determined. Finally, the exact mechanisms of protection by our vaccine remain incompletely defined. Live-attenuated vaccines can elicit both strong antibody and cytotoxic T-cell responses. Although cell-mediated immune responses were not specifically measured in this study, these activities likely contributed to protection, and the magnitude and nature of such responses will need to be examined further.

Important caveats for the vaccine described in the current study include that the insertion of the RBD antigen was associated with a reduction in viral yield, and our method of inactivation was formalin fixation rather than detergent treatment. Additional studies will be required to understand how fixation conditions may affect immunogenicity and how decreased yield would affect the eventual vaccine cost or timelines for manufacturing. Finally, we have only utilized one genetic background and corresponding set of viral glycoproteins for these studies. While A/Puerto Rico/8/1934 is a standard background for vaccine development, it will also be important to understand if other H1 (or H3/influenza B virus) HA proteins are amenable to our manipulations to segment length and composition such that a membrane-anchored RBD domain can be functionally encoded.

In conclusion, the influenza-based, multivalent vaccines may represent a generalizable approach to reduce the time and manufacturing requirements for development of novel vaccines. Since the current influenza vaccine is composed of three or four

distinct strains (5), this approach could be even more multiplexed to elicit responses against more than two pathogens or multiple strains of the same pathogen. While there remain questions to be answered and technical challenges to overcome, influenza virus-based vaccines may be an attractive approach to produce and package antigens that are difficult to purify or are poorly immunogenic on their own. Continued work on this and other generalizable vaccine platforms will not only help with the current response to the COVID-19 pandemic but will help poise us for rapid response during future epidemic/pandemic outbreaks.

MATERIALS AND METHODS

Cell lines and viruses. Human embryonic kidney cells (HEK293T; ATCC) and human lung carcinoma (A549) cells with or without hACE2 were grown in Dulbecco's modified Eagle medium supplemented with 5% fetal bovine serum (GlutaMAX; Gibco catalog [cat.] no. 35050079) and penicillin/streptomycin. Madin-Darby canine kidney cells (MDCK; ATCC) were grown in minimum essential medium (MEM) supplemented with 5% fetal bovine serum (FBS; GlutaMAX), HEPES, NaHCO$_3$, and penicillin/streptomycin. African green monkey kidney cells (Vero E6; ATCC) were grown in MEM plus Earl's salts plus L-glutamine (Gibco; 11095-080). This medium was supplemented with penicillin/streptomycin, 10% FBS, 1 mM sodium pyruvate, and 1× MEM non-essential amino acids (NEAA) (Gibco; 11140-050). ST cells (ATCC; CRL-1746) were grown in Eagle's Minimum Essential Media (EMEM) supplemented with penicillin/streptomycin and 10% FBS. All cells were grown at 37°C under 5% CO$_2$. The A/Puerto Rico/8/1934 (PR8) virus genetic backbone was used for vaccine development, and corresponding unmodified virus was used for vaccination/animal challenge experiments. SARS-related coronavirus 2, isolate USA-WA1/2020, NR-52281, was used for SARS-CoV-2 infections and is from BEI Resources. To account for any potential mutations in viral genomes selected for during strain propagation, each genomic segment of all strains used for challenge in this study were subjected to Sanger sequencing. GenBank accession numbers for the A/Puerto Rico/8/1934 viral genes (with mutations noted in brackets) are the following: AF389115 (PB2), CY148249 (PB1 [A549C→K175N]), AF389117 (PA [A1025T→Y334F]), AF389118 (HA), AF389119 (NP), AF389120 (NA), AF389121 (M), and AF389122 (NS). GenBank accession numbers and mutations for the TM-RBD-HA vaccine virus are the following: AF389115 (PB2), CY148249 (PB1 [A549C→K175N]), AF389117 (PA [A1025T→Y334F]), AF389118 (HA [G1456A→E451K, A1683G→I526M]), AF389119 (NP [C515T→T157I]), AF389120 (NA), AF389121 (M [T1027A→silent]), and AF389122 (NS).

Cloning and rescue of A/Puerto Rico/8/1934 encoding SARS-CoV-2 RBD. Influenza segment cloning was accomplished as previously described (30). First, the RBD, which includes amino acids 319 to 541 of the spike protein ORF, from the SARS-CoV-2 Wuhan-Hu-1 isolate (accession no. MN908947.3) was codon optimized for expression in influenza A viruses and synthesized by Integrated DNA Technologies (IDT). Importantly, we also encoded the NA transmembrane domain (amino acids 1 to 40 of the NA ORF) 5′ to the RBD to allow it to be incorporated into the viral particle and encoded a FLAG tag 3′ to the RBD to aid in detection as needed. Once this was done, the codon-optimized RBD was PCR amplified and cloned into the bicistronic pDZ rescue plasmid system for A/Puerto Rico/8/1934 using the NEBuilder HiFi DNA assembly kit (New England Biolabs [NEB]). Specifically, the SARS-CoV-2 TM-RBD construct was cloned into the previously reported mNeon-HA construct, wherein the TM-RBD sequence replaced the mNeon reporter, allowing expression of the transgene 5′ to the HA (30). Successful cloning was then confirmed by Sanger sequencing. Viral rescue was then performed by transfecting the modified TM-RBD-HA plasmid alongside the 7 plasmids encoding the other PR8 segments into 293Ts using the Mirus TransIT-LT1 reagent. Rescued virus was then amplified via inoculation of virus into 10-day-old embryonated chicken eggs (Charles River) at 37°C for 3 days and plaque purified, and the individual plaque was amplified in 10-day-old embryonated chicken eggs again.

Virus propagation and growth kinetics. Influenza virus titering was performed as previously reported (30). For virus propagation, approximately 500 PFU of each plaque-purified stock was injected in 10-day-old embryonated hen eggs purchased from Charles River Laboratories, Inc., and incubated for 72 h at 37°C. The allantoic fluid was then harvested, and the titer was determined via plaque assay on MDCK cells. This was accomplished by serially diluting allantoic fluid and then incubating MDCKs with 500 μL of the diluted sample for 1 h at 37°C. After incubation, the viral suspension was aspirated, agar overlay was applied, and cells were incubated at 37°C for 48 to 72 h depending on plaque size. Plaque assays were then fixed by adding 2 mL of 4% formaldehyde solution and incubating the mixture overnight at room temperature. The next day formaldehyde was aspirated, and cells were washed prior to antigen staining to detect viral protein. For antigen staining, fixed monolayers stained with a 1:2,000 dilution of vaccinated mouse serum in antibody dilution buffer (5% milk, 0.05% Tween 20 in phosphate-buffered saline [PBS]). Plaque assays were incubated at 4°C for 2 h/overnight and then stained with a 1:4,000 dilution of horseradish peroxidase (HRP)-conjugated anti-mouse secondary antibody (Novex cat. no. NXA931V) for 2 h at room temperature. Plaque assays were developed with 0.5 mL of the TrueBlue peroxidase substrate (KPL). For viral growth curves and endpoint titer assays, eggs were injected with 10,000 PFU/egg, and eggs were collected for plaque assay at 24, 48, and 72 h postinfection. Hemagglutination assays were performed by serially diluting virus 1:2 in PBS in a 96-well plate and then adding chicken blood to each well. Plates were incubated 1 h, and then each well was scored as positive or negative.

SARS-CoV-2 stocks for *in vitro* assays were grown on Vero E6 cells in virus infection medium (MEM plus Earl's salts, penicillin/streptomycin, 2% FBS, 1 mM sodium pyruvate, and 1× MEM NEAA) for 72 h. Stocks

were frozen at −80°C and were titered by serially diluting virus in virus infection medium and then infecting a confluent monolayer of Vero E6 cells growing in 6-well, poly-L-lysine-treated plates for 1 h. Inoculum was then removed, and an agarose overlay was added. Cells were incubated at 37°C and 5% CO_2 for 72 h and then were stained with 0.05% neutral red in PBS for 3 h. SARS-CoV-2 stocks for animal infections were grown on ST cells in virus infection medium. Virus was titered using a similar protocol as above; however, using a methylcellulose overlay, virus was incubated for 4 days, and monolayers were stained with crystal violet.

Viral purification. Influenza virus was purified for use in both vaccination and ELISAs. First, viral stocks were grown in 10-day-old embryonated chicken eggs as described above. Then allantoic fluid was collected and dialyzed overnight using Spectra-Por Float-A-Lyzer G2 10-mL, 100-kDa molecular weight cutoff (MWCO) tubes according to the manufacturer's instructions (Millipore Sigma cat. no. Z727253-12EA). After samples were dialyzed to remove larger impurities, the allantoic fluid was collected, and virus samples were concentrated by ultracentrifugation using a 30% sucrose cushion for 1 h at 25,700 rpm using the Sorvall TH-641 swinging bucket rotor. Virus samples were then resuspended in PBS and pooled prior to being fixed in 0.02% formalin for 30 min at room temperature. Samples were then once again dialyzed overnight to remove formalin using Slide-A-Lyzer cassettes (Thermo Scientific cat. no. PI66370) before being stored at 4°C until use.

RT-PCR and serial passage experiments. For serial passage experiments, an 80% confluent monolayer of MDCK cells was infected with the appropriate virus at a multiplicity of infection (MOI) of 0.01 for 48 h. Cell supernatants were then collected and centrifuged for 5 min at 500 × *g*. The supernatants were then removed, and 100 μL was added to 1 mL of TRIzol and frozen at −80°C. The titer of the remaining virus was then estimated by hemagglutination assay, and a new monolayer of cells was subsequently infected. This protocol was repeated 10 times. For analysis, viral RNA was extracted via TRIzol (Invitrogen) followed by chloroform/ethanol precipitation or using Qiagen viral RNA miniprep kits. RT-PCRs were performed using SuperScript III one-step RT-PCR system kits (Thermo cat. no. 12574026) according to the manufacturer's guidelines. The primers used were HA 5′ forward, 5′-GTAGATGCAGCAAAAGCAGGGGAAAATA-3′; HA 3′ reverse, 5′-CCATCCTCAATTTGGCAC-3′; RC093, 5′-AGCAAAAGCAGGGGAAAATA-3′; and RC095, 5′-GTCTTC GAGCAGGTTAACAG-3′. RT-PCRs using RNA generated from miniprep kits varied in template concentration, as the presence of carrier RNA inhibits nucleic acid quantification via photometric means. RT-PCR products were analyzed on 0.8 to 1% agarose gels run at 50 V.

Microscopy. MDCK cells were seeded in 24-well plates containing glass coverslips coated with poly-L-lysine and allowed to grow at 37°C for 24 h prior to infection. Cells were washed with PBS and infected with either PR8 or TM-RBD-HA virus at an MOI of 0.25 in infection medium (1 mM KH_2PO_4, 155 mM NaCl, Na_2HPO_4, 83.5 mM $CaCl_2$, 105 mM $MgCl_2$, 10 U/mL penicillin/streptomycin, 0.4% BSA) for 1 h at 37°C. Virus was removed from cells and replaced with postinfection medium (Gibco Opti-MEM supplemented with 0.01% FBS, 10 U/mL penicillin/streptomycin, 0.4% BSA, and 1 μg/mL N-tosyl-L-phenylalanine chloromethyl ketone (TPCK)-trypsin). Cells were incubated for 24 h and fixed with methanol-free 4% formaldehyde (Fischer cat. no. PI28906). DNA was visualized using Hoechst 33342 (Thermo) at 5 μg/mL in PBS for 15 min. HA and SARS-CoV-2 were detected using PY102 and SARS-CoV-2 spike protein (RBD) polyclonal antibody (Thermo cat. no. PA5-114451), respectively, at a 1:250 dilution for approximately 3 h. Primary antibodies were visualized using AlexFluor594-conjugated anti-mouse (for HA) and AlexFluor488-conjugated anti-rabbit (for RBD) secondary antibodies (Thermo cat. no. A-11032/A-11008) at a dilution of 1:500 for 1 h at room temperature. Cells were imaged on a ZOE (Bio-Rad) microscope.

Western blots. Protein extracts were quantified and normalized via Bradford assay. SDS-PAGE was performed using 4 to 20% polyacrylamide gels (Bio-Rad) electrophoresed at 120 V for 60 min. Proteins were transferred to 0.45-μm nitrocellulose membranes at 90 V for 60 min at 4°C and blocked using PBS with Tween 20 (PBST) plus 5% milk for a minimum of 1 h at room temperature. For cellular lysates, 20 μg of total protein was loaded per sample. To normalize viral protein extracts, 0.5 μg of PR8 and PR8-TM-RBD HA were initially loaded and analyzed via Western blotting. Viral protein extracts were probed for M1 and normalized via densitometry (ImageJ; NIH). After normalization to M1, 0.5 μg PR8 and 1.32 μg PR8-TM-RBD HA were loaded for subsequent Western blot analyses. The following antibodies were used for protein detection: PY102 (HA, 1 μg/mL), 4A5 (NA, 0.45 μg/mL), anti-matrix protein (E10) (M1 and M2, 1:1,000; Kerafast cat. no. EMS009), and anti-SARS-CoV-2 spike protein (RBD) polyclonal antibody (RBD, 1:1,000; Invitrogen cat. no. PA5-114451). All primary antibodies were diluted in PBST plus 5% milk and applied to membranes for ≥16 h at 4°C. Anti-mouse (1:20,000; Thermo cat. no. A16072) and anti-rabbit (1:10,000; Thermo cat. no. A16104) secondary antibodies were diluted in PBST plus 5% milk and applied to membranes for 60 min at room temperature. Membranes were developed using Clarity ECL or Clarity ECL MAX.

Purification of soluble HA, NA, and RBD proteins for ELISAs. The 6×-His-tagged proteins were overexpressed in Expi293F cells (Thermo cat. no. A14527) via transfection of expression vectors. Cells were lysed via sonication, and clarified lysates were applied to Ni-NTA columns. Eluted protein fractions were combined, dialyzed, and stored at −80°C.

ELISAs. Proteins/viruses were immobilized to 96-well plates using carbonate coating buffer (30 mM Na_2CO_3, 70 mM $NaHCO_3$, pH 9.5) for ≥16 h at 4°C. For protein samples, 50 to 100 μL of sample at 10 μg/mL was added to wells. For viral samples, 1×10^6 PFU were added to wells in a volume of 50 to 100 μL. All samples were diluted using PBS plus 3% BSA. After coating, wells were washed with PBS and blocked with PBS plus 3% BSA for at least 1 h at room temperature. Primary antibodies were diluted using PBS plus 3% BSA and incubated with immobilized proteins/viruses for ≥1 h at room temperature (anti-RBD, ProSci cat. no. 9087; anti-HA PY102, a kind gift from Tom Moran [Icahn School of Medicine at Mount Sinai]; DH1041 and DH1044, a kind gift from Bart Haynes, Kevin Saunders, and Dapeng Li [Duke]). Anti-human (1:10,000; Thermo cat. no. A18805), anti-mouse (1:5,000; Thermo cat. no. A16072), and anti-

rabbit (1:5,000; Thermo cat. no. A16104) secondary antibodies were diluted in PBS plus 3% BSA and incubated with immobilized proteins/virus for 1 h at room temperature. ELISAs were developed using 1-Step Ultra tetramethylbenzidine (TMB)-ELISA substrate (Thermo cat. no. 34029) and quenched with 2 M H_2SO_4.

Animal infections/live-attenuated vaccination. Animal infections were performed using age-matched C57BL/6J (Jackson Laboratory 000664) or B6.Cg-Tg(K18-*ACE2*)2Prlmn/J mice (Jackson Laboratory 034860) in accordance with Duke University Institutional Animal Care and Use Committee (IACUC)-approved protocol no. A189-18-08 and A081-20-04. For influenza infections, mice were anesthetized using 100 μL of a 14.2-mg/mL ketamine-xylazine mixture via intraperitoneal injection. After administration of anesthesia, mouse tails were marked or mice were injected subcutaneously with IPT-300 transponders capable of reading body temperature and animal ID (BMDS IPT-300), and baseline weights and temperatures were measured. For Fig. 3F and G, mice were inoculated with 40 μL of the indicated dose of virus diluted in pharmaceutical-grade PBS. Body weight was measured daily, and mice were euthanized if their body weight reached 75% of baseline. For vaccinations using inactivated virus, 10 μg virus or BSA was injected via the intramuscular (i.m.) route. For live-attenuated vaccinations, mice were given a 40-μL intranasal inoculum of virus or PBS control, either 10 to 15 PFU WT A/Puerto Rico/8/1934 or 100-250 PFU TM-RBD-HA diluted in pharmaceutical-grade PBS. Vaccination doses varied depending on which stock was used. For mice receiving a boost, another 10 μg of inactivated virus or BSA control was administered via the i.m. route. For challenge experiments, mice were inoculated with 500 PFU of PR8. After infection, mice were weighed daily and euthanized if their body weight reached 75% of the baseline weight. This cutoff was determined relative to the weight prior to infection. Euthanasia was performed via a primary method of CO_2 asphyxiation and bilateral thoracotomy as a secondary confirmation. These methods were used during both challenge experiments and administration of the live virus vaccine prime. For SARS-CoV-2 challenge experiments, prior to infection, mice were injected subcutaneously with IPT-300 transponders, and baseline weights and temperatures were measured. On the day of infection, mice were anesthetized using isoflurane and then given a 50-μL intranasal inoculum of virus, 3×10^4 PFU, diluted in pharmaceutical-grade PBS. After infection, mice were monitored daily for weight, temperature, and clinical signs (temperature and clinical signs not reported). Mice were euthanized via CO_2 asphyxiation and bilateral thoracotomy as a secondary confirmation when their body weight reached 80% of the baseline weight measured prior to infection or reached a clinical score of 4 in accordance with the approved protocol mentioned above (A081-20-04). Occasionally, mice did not recover from anesthesia, and these animals were excluded from subsequent experimentation and analysis.

Vaccination of mice with inactivated virus. Vaccine doses for the boost were prepared using the purified inactivated virus described above. Virus samples were then diluted 1:1 with the adjuvant AddaVax (InvivoGen cat. no. vac-adx-10) to a final concentration of 100 μg/mL. After preparation of doses, mice were anesthetized as described above and then administered a 100-μL injection intramuscularly into the left leg. Mice were then monitored the next day for side effects and then housed for the indicated period of time before collection or viral challenge. If serum was collected, mice were anesthetized, and then blood was harvested either by cheek bleed or terminal bleed, and serum was collected using Sarstedt Z-Gel tubes according to the manufacturer's instructions (Sarstedt cat. no. 41.1378.005). Serum was then stored at $-80°C$ until use.

Histological analysis and viral burden quantification in mouse lungs. To quantify the PFU of influenza virus or SARS-CoV-2 in the lungs of mice, lungs were collected 5 days postinfection. Lungs were placed in PBS and homogenized using Benchmark BeadBlaster 24 microtube homogenizer or Benchmark BeadBug homogenizer. Homogenates were centrifuged and supernatants were removed and frozen at $-80°C$. PFU were quantified by diluting homogenates and performing plaque assays as described above. For histology experiments, mice were anesthetized with 200 μL of ketamine-xylazine prior to cervical dislocation. The lungs were inflated with 1.5 mL of 4% formaldehyde solution, and the trachea was tied off with suture string before removal. The inflated lungs were stored in 4% formaldehyde at room temperature until they were processed for histology. Histology was performed by HistoWiz, Inc. (histowiz.com), using a standard operating procedure and fully automated workflow. Samples were processed, embedded in paraffin, and sectioned at 4 μm. Staining was performed on a BOND RX autostainer (Leica Biosystems) using standard protocols. Whole-slide scanning was performed on an Aperio AT2 instrument (Leica Biosystems). Images shown are at $\times$10 and $\times$40 magnification.

Pseudotyped lentivirus transduction experiments. The SARS-CoV-2 RBD ORF was cloned into the pCAGGS expression plasmid. To package lentivirus particles, combinations of pCAGGS-RBD, pNL4-3.Luc, $p\Delta8.74$, pDZ-HA, and pDZ-NA were transfected into 293T cells using polyethylenimine (PEI) incubated at 37°C for 72 h. For pseudotyped viral particles, 293Ts were grown in serum-free Opti-MEM growth medium. Pseudotyped viruses were harvested and stored at $-80°C$. For transduction experiments, A549 and A549-*ACE2* cells were plated in 24-well plates. To transduce cells, 100 μL of medium containing pseudotyped viruses was added to each culture and incubated at 37°C for 48 h. Transduction efficiency was determined via luciferase assays using a firefly luciferase detection kit (Promega cat. no E1500). Luciferase intensities were measured using a luminometer. pNL4-3.Luc and $p\Delta8.74$ plasmids were a kind gift from Bryan Cullen (Duke University).

SialidaseA treatment of cells. SialidaseA (Agilent cat. no. GK80040) was used to cleave α2,3- and α2,6-N-linked sialic acids from the surfaces of cells. Briefly, growth medium was supplemented with SialidaseA at 30 mU/mL, and this supplemented medium was used to exchange the medium on cells. Cells were incubated with SialidaseA-containing medium for 3 to 5 h at 37°C. After incubation, medium was removed, and cells were washed with PBS to remove residual SialidaseA. Cells were subsequently infected with either WT or TM-RBD-HA virus (MOI = 1) for 1 h. Cells were grown in complete growth medium and fixed with 4% paraformaldehyde after 24 h. Virus-infected cells were detected using PY102

antibody (1:2,000), stained using TrueBlue peroxidase substrate (KPL), and imaged on a ZOE microscope (Bio-Rad). The number of infected cells per field of view was determined using FIJI (NIH); image threshold values were set to 0 to 85, and particles (size, 1,000 to 1,000,000 px; circularity, 0 to infinity) were counted. Five nonoverlapping areas of each well were imaged and used for quantification.

Plaque reduction neutralization assays. MDCK and Vero cells were used for influenza and SARS-CoV-2 plaque reduction assays, respectively. A master mix of virus was diluted to the indicated concentration ($\sim$40 to 80 PFU/mL) and aliquoted prior to being mixed with antibody dilutions (from sera or purified monoclonal antibodies). Following a 45-minute incubation at room temperature with antibody, the medium was aspirated from cells, and 500 μL of the virus-antibody mixture was added to each well of cells. For each experiment a no-antibody control was included to accurately record how much virus had been used to infect cells. Cells were incubated with the virus-antibody mixture at 37°C for 1 h, rocking the samples every 15 min to ensure cells were completely covered by the solution. After this period, the solution was aspirated, and an agar overlay was applied. For influenza plaque reduction assays, staining and plaque counting were performed as described above in the titering section. SARS-CoV-2 plaque reduction assays were evaluated by first staining plaques with 0.05% neutral red solution for 3 h at 37°C (Sigma-Aldrich cat. no. N2889-100mL). Neutral red was then aspirated from the wells, and plaques were counted. The percent reduction in plaques was calculated in reference to a no-serum control. The reciprocal 50% neutralization titer was calculated by averaging the greatest dilution of mouse sera that had a $>$50% reduction in plaques compared to a no-serum control for each serum sample in a vaccination group.

Statistical analysis. Data were analyzed and presented using GraphPad Prism software. Statistical tests that were applied to each experiment are denoted in the appropriate figure legend. For all bar plots, unpaired Mann-Whitney tests were used. For survival plots, Mantel-Cox tests were used. All experiments were performed using a minimum of 4 samples, unless otherwise noted.

REFERENCES

1. Harding AT, Heaton NS. 2018. Efforts to improve the seasonal influenza vaccine. Vaccines 6:19. https://doi.org/10.3390/vaccines6020019.
2. Trombetta CM, Gianchecchi E, Montomoli E. 2018. Influenza vaccines: evaluation of the safety profile. Hum Vaccin Immunother 14:657–670. https://doi.org/10.1080/21645515.2017.1423153.
3. Savidan E, Chevat C, Marsh G. 2008. Economic evidence of influenza vaccination in children. Health Policy 86:142–152. https://doi.org/10.1016/j.healthpol.2007.09.009.
4. Sullivan SG, Price OH, Regan AK. 2019. Burden, effectiveness and safety of influenza vaccines in elderly, paediatric and pregnant populations. Ther Adv Vaccines Immunother 7:2515135519826481. https://doi.org/10.1177/2515135519826481.
5. Wei CJ, Crank MC, Shiver J, Graham BS, Mascola JR, Nabel GJ. 2020. Next-generation influenza vaccines: opportunities and challenges. Nat Rev Drug Discov 19:239–252. https://doi.org/10.1038/s41573-019-0056-x.
6. Sridhar S, Brokstad KA, Cox RJ. 2015. Influenza vaccination strategies: comparing inactivated and live attenuated influenza vaccines. Vaccines (Basel) 3:373–389. https://doi.org/10.3390/vaccines3020373.
7. Hoft DF, Babusis E, Worku S, Spencer CT, Lottenbach K, Truscott SM, Abate G, Sakala IG, Edwards KM, Creech CB, Gerber MA, Bernstein DI, Newman F, Graham I, Anderson EL, Belshe RB. 2011. Live and inactivated influenza vaccines induce similar humoral responses, but only live vaccines induce diverse T-cell responses in young children. J Infect Dis 204:845–853. https://doi.org/10.1093/infdis/jir436.
8. Zens KD, Chen JK, Farber DL. 2016. Vaccine-generated lung tissue-resident memory T cells provide heterosubtypic protection to influenza infection. JCI Insight 1:e85832. https://doi.org/10.1172/jci.insight.85832.
9. Sasaki S, Jaimes MC, Holmes TH, Dekker CL, Mahmood K, Kemble GW, Arvin AM, Greenberg HB. 2007. Comparison of the influenza virus-specific effector and memory B-cell responses to immunization of children and adults with live attenuated or inactivated influenza virus vaccines. J Virol 81:215–228. https://doi.org/10.1128/JVI.01957-06.
10. Nogales A, Martinez-Sobrido L. 2016. Reverse genetics approaches for the development of influenza vaccines. Int J Mol Sci 18:20. https://doi.org/10.3390/ijms18010020.
11. Fiege JK, Langlois RA. 2015. Investigating influenza A virus infection: tools to track infection and limit tropism. J Virol 89:6167–6170. https://doi.org/10.1128/JVI.00462-15.

12. Dumm RE, Heaton NS. 2019. The development and use of reporter influenza B viruses. Viruses-Basel 11 11:736. https://doi.org/10.3390/v11080736.

13. Jenkins MR, Webby R, Doherty PC, Turner SJ. 2006. Addition of a prominent epitope affects influenza A virus-specific CD8(+) T cell immunodominance hierarchies when antigen is limiting. J Immunol 177:2917–2925. https://doi.org/10.4049/jimmunol.177.5.2917.

14. Li J, Arevalo MT, Zeng M. 2013. Engineering influenza viral vectors. Bioengineered 4:9–14. https://doi.org/10.4161/bioe.21950.

15. Hu B, Guo H, Zhou P, Shi ZL. 2021. Characteristics of SARS-CoV-2 and COVID-19. Nat Rev Microbiol 19:141–154. https://doi.org/10.1038/s41579-020-00459-7.

16. Dong Y, Dai T, Wei Y, Zhang L, Zheng M, Zhou F. 2020. A systematic review of SARS-CoV-2 vaccine candidates. Signal Transduct Target Ther 5:237. https://doi.org/10.1038/s41392-020-00352-y.

17. Sadoff J, Le Gars M, Shukarev G, Heerwegh D, Truyers C, de Groot AM, Stoop J, Tete S, Van Damme W, Leroux-Roels I, Berghmans PJ, Kimmel M, Van Damme P, de Hoon J, Smith W, Stephenson KE, De Rosa SC, Cohen KW, McElrath MJ, Cormier E, Scheper G, Barouch DH, Hendriks J, Struyf F, Douoguih M, Van Hoof J, Schuitemaker H. 2021. Interim results of a phase 1-2a trial of Ad26.COV2.S covid-19 vaccine. N Engl J Med 384:1824–1835. https://doi.org/10.1056/NEJMoa2034201.

18. Baden LR, El Sahly HM, Essink B, Kotloff K, Frey S, Novak R, Diemert D, Spector SA, Rouphael N, Creech CB, McGettigan J, Khetan S, Segall N, Solis J, Brosz A, Fierro C, Schwartz H, Neuzil K, Corey L, Gilbert P, Janes H, Follmann D, Marovich M, Mascola J, Polakowski L, Ledgerwood J, Graham BS, Bennett H, Pajon R, Knightly C, Leav B, Deng W, Zhou H, Han S, Ivarsson M, Miller J, Zaks T, COVE Study Group. 2021. Efficacy and safety of the mRNA-1273 SARS-CoV-2 vaccine. N Engl J Med 384:403–416. https://doi.org/10.1056/NEJMoa2035389.

19. Polack FP, Thomas SJ, Kitchin N, Absalon J, Gurtman A, Lockhart S, Perez JL, Perez Marc G, Moreira ED, Zerbini C, Bailey R, Swanson KA, Roychoudhury S, Koury K, Li P, Kalina WV, Cooper D, Frenck RW, Jr, Hammitt LL, Tureci O, Nell H, Schaefer A, Unal S, Tresnan DB, Mather S, Dormitzer PR, Sahin U, Jansen KU, Gruber WC, C4591001 Clinical Trial Group. 2020. Safety and efficacy of the BNT162b2 mRNA Covid-19 vaccine. N Engl J Med 383:2603–2615. https://doi.org/10.1056/NEJMoa2034577.

20. Rubin R. 2021. COVID-19 vaccines vs variants-determining how much immunity is enough. JAMA 325:1241. https://doi.org/10.1001/jama.2021.3370.

21. Mlcochova P, Kemp SA, Dhar MS, Papa G, Meng B, Ferreira IATM, Datir R, Collier DA, Albecka A, Singh S, Pandey R, Brown J, Zhou J, Goonawardane N, Mishra S, Whittaker C, Mellan T, Marwal R, Datta M, Sengupta S, Ponnusamy K, Radhakrishnan VS, Abdullahi A, Charles O, Chattopadhyay P, Devi P, Caputo D, Peacock T, Wattal C, Goel N, Satwik A, Vaishya R, Agarwal M, Mavousian A, Lee JH, Bassi J, Silacci-Fegni C, Saliba C, Pinto D, Irie T, Yoshida I, Hamilton WL, Sato K, Bhatt S, Flaxman S, James LC, Corti D, Piccoli L, Barclay WS, Rakshit P, CITIID-NIHR BioResource COVID-19 Collaboration, et al. 2021. SARS-CoV-2 B.1.617.2 Delta variant replication and immune evasion. Nature 599:114–119. https://doi.org/10.1038/s41586-021-03944-y.

22. Zhang L, Li Q, Liang Z, Li T, Liu S, Cui Q, Nie J, Wu Q, Qu X, Huang W, Wang Y. 2022. The significant immune escape of pseudotyped SARS-CoV-2 variant Omicron. Emerg Microbes Infect 11:1–5. https://doi.org/10.1080/22221751.2021.2017757.

23. Honda-Okubo Y, Barnard D, Ong CH, Peng BH, Tseng CT, Petrovsky N. 2015. Severe acute respiratory syndrome-associated coronavirus vaccines formulated with delta inulin adjuvants provide enhanced protection while ameliorating lung eosinophilic immunopathology. J Virol 89:2995–3007. https://doi.org/10.1128/JVI.02980-14.

24. Poland GA, Ovsyannikova IG, Kennedy RB. 2020. SARS-CoV-2 immunity: review and applications to phase 3 vaccine candidates. Lancet 396:1595–1606. https://doi.org/10.1016/S0140-6736(20)32137-1.

25. Sariol A, Perlman S. 2020. Lessons for COVID-19 immunity from other coronavirus infections. Immunity 53:248–263. https://doi.org/10.1016/j.immuni.2020.07.005.

26. Huang AT, Garcia-Carreras B, Hitchings MDT, Yang B, Katzelnick LC, Rattigan SM, Borgert BA, Moreno CA, Solomon BD, Trimmer-Smith L, Etienne V, Rodriguez-Barraquer I, Lessler J, Salje H, Burke DS, Wesolowski A, Cummings DAT. 2020. A systematic review of antibody mediated immunity to coronaviruses: kinetics, correlates of protection, and association with severity. Nat Commun 11:4704. https://doi.org/10.1038/s41467-020-18450-4.

27. Lan J, Ge JW, Yu JF, Shan SS, Zhou H, Fan SL, Zhang Q, Shi XL, Wang QS, Zhang LQ, Wang XQ. 2020. Structure of the SARS-CoV-2 spike receptor-binding domain bound to the ACE2 receptor. Nature 581:215–220. https://doi.org/10.1038/s41586-020-2180-5.

28. Tai WB, He L, Zhang XJ, Pu J, Voronin D, Jiang SB, Zhou YS, Du LY. 2020. Characterization of the receptor-binding domain (RBD) of 2019 novel

coronavirus: implication for development of RBD protein as a viral attachment inhibitor and vaccine. Cell Mol Immunol 17:613–620. https://doi.org/10.1038/s41423-020-0400-4.

29. Soema PC, Kompier R, Amorij JP, Kersten GF. 2015. Current and next generation influenza vaccines: formulation and production strategies. Eur J Pharm Biopharm 94:251–263. https://doi.org/10.1016/j.ejpb.2015.05.023.

30. Harding AT, Heaton BE, Dumm RE, Heaton NS. 2017. Rationally designed influenza virus vaccines that are antigenically stable during growth in eggs. mBio 8:e00669-17. https://doi.org/10.1128/mBio.00669-17.

31. Heaton NS, Leyva-Grado VH, Tan GS, Eggink D, Hai R, Palese P. 2013. In vivo bioluminescent imaging of influenza a virus infection and characterization of novel cross-protective monoclonal antibodies. J Virol 87:8272–8281. https://doi.org/10.1128/JVI.00969-13.

32. Dumm RE, Fiege JK, Waring BM, Kuo CT, Langlois RA, Heaton NS. 2019. Non-lytic clearance of influenza B virus from infected cells preserves epithelial barrier function. Nat Commun 10:779. https://doi.org/10.1038/s41467-019-08617-z.

33. Beare AS, Schild GC, Craig JW. 1975. Trials in man with live recombinants made from A/Pr/8/34 (H0 N1) and wild H-3 N2 influenza-viruses. Lancet 306:729–732. https://doi.org/10.1016/S0140-6736(75)90720-5.

34. Selzer L, Su ZM, Pintilie GD, Chiu W, Kirkegaard K. 2020. Full-length three-dimensional structure of the influenza A virus M1 protein and its organization into a matrix layer. PLoS Biol 18:e3000827. https://doi.org/10.1371/journal.pbio.3000827.

35. Li D, Edwards RJ, Manne K, Martinez DR, Schafer A, Alam SM, Wiehe K, Lu X, Parks R, Sutherland LL, Oguin TH, 3rd, McDanal C, Perez LG, Mansouri K, Gobeil SMC, Janowska K, Stalls V, Kopp M, Cai F, Lee E, Foulger A, Hernandez GE, Sanzone A, Tilahun K, Jiang C, Tse LV, Bock KW, Minai M, Nagata BM, Cronin K, Gee-Lai V, Deyton M, Barr M, Von Holle T, Macintyre AN, Stover E, Feldman J, Hauser BM, Caradonna TM, Scobey TD, Rountree W, Wang Y, Moody MA, Cain DW, DeMarco CT, Denny TN, Woods CW, Petzold EW, Schmidt AG, Teng IT, et al. 2021. In vitro and in vivo functions of SARS-CoV-2 infection-enhancing and neutralizing antibodies. Cell 184:4203–4219.e32. https://doi.org/10.1016/j.cell.2021.06.021.

36. Saunders KO, Lee E, Parks R, Martinez DR, Li D, Chen H, Edwards RJ, Gobeil S, Barr M, Mansouri K, Alam SM, Sutherland LL, Cai F, Sanzone AM, Berry M, Manne K, Bock KW, Minai M, Nagata BM, Kapingidza AB, Azoitei M, Tse LV, Scobey TD, Spreng RL, Rountree RW, DeMarco CT, Denny TN, Woods CW, Petzold EW, Tang J, Oguin TH, III, Sempowski GD, Gagne M, Douek DC, Tomai MA, Fox CB, Seder R, Wiehe K, Weissman D, Pardi N, Golding H, Khurana S, Acharya P, Andersen H, Lewis MG, Moore IN, Montefiori DC, Baric RS, Haynes BF. 2021. Neutralizing antibody vaccine for pandemic and pre-emergent coronaviruses. Nature 594:553–559. https://doi.org/10.1038/s41586-021-03594-0.

37. Weis W, Brown JH, Cusack S, Paulson JC, Skehel JJ, Wiley DC. 1988. Structure of the influenza virus haemagglutinin complexed with its receptor, sialic acid. Nature 333:426–431. https://doi.org/10.1038/333426a0.

38. Winkler ES, Bailey AL, Kafai NM, Nair S, McCune BT, Yu JS, Fox JM, Chen RE, Earnest JT, Keeler SP, Ritter JH, Kang LI, Dort S, Robichaud A, Head R, Holtzman MJ, Diamond MS. 2020. Publisher Correction: SARS-CoV-2 infection of human ACE2-transgenic mice causes severe lung inflammation and impaired function. Nat Immunol 21:1470. https://doi.org/10.1038/s41590-020-0794-2.

39. Okamoto S, Matsuoka S, Takenaka N, Haredy AM, Tanimoto T, Gomi Y, Ishikawa T, Akagi T, Akashi M, Okuno Y, Mori Y, Yamanishi K. 2012. Intranasal immunization with a formalin-inactivated human influenza A virus whole-virion vaccine alone and intranasal immunization with a split-virion vaccine with mucosal adjuvants show similar levels of cross-protection. Clin Vaccine Immunol 19:979–990. https://doi.org/10.1128/CVI.00016-12.

40. Belshe RB, Edwards KM, Vesikari T, Black SV, Walker RE, Hultquist M, Kemble G, Connor EM, CAIV-T Comparative Efficacy Study Group. 2007. Live attenuated versus inactivated influenza vaccine in infants and young children. N Engl J Med 356:685–696. https://doi.org/10.1056/NEJMoa065368.

41. Sparrow E, Wood JG, Chadwick C, Newall AT, Torvaldsen S, Moen A, Torelli G. 2021. Global production capacity of seasonal and pandemic influenza vaccines in 2019. Vaccine 39:512–520. https://doi.org/10.1016/j.vaccine.2020.12.018.

42. Pena L, Sutton T, Chockalingam A, Kumar S, Angel M, Shao HX, Chen HJ, Li WZ, Perez DR. 2013. Influenza viruses with rearranged genomes as live-attenuated vaccines. J Virol 87:5118–5127. https://doi.org/10.1128/JVI.02490-12.

43. Gao Q, Lowen AC, Wang TT, Palese P. 2010. A nine-segment influenza a virus carrying subtype H1 and H3 hemagglutinins. J Virol 84:8062–8071. https://doi.org/10.1128/JVI.00722-10.

44. Sereinig S, Stukova M, Zabolotnyh N, Ferko B, Kittel C, Romanova J, Vinogradova T, Katinger H, Kiselev O, Egorov A. 2006. Influenza virus NS vectors expressing the mycobacterium tuberculosis ESAT-6 protein induce CD4+ Th1 immune response and protect animals against tuberculosis challenge. Clin Vaccine Immunol 13:898–904. https://doi.org/10.1128/CVI.00056-06.

45. He Q, Martinez-Sobrido L, Eko FO, Palese P, Garcia-Sastre A, Lyn D, Okenu D, Bandea C, Ananaba GA, Black CM, Igietseme JU. 2007. Live-attenuated influenza viruses as delivery vectors for Chlamydia vaccines. Immunology 122:28–37. https://doi.org/10.1111/j.1365-2567.2007.02608.x.

46. Loes AN, Gentles LE, Greaney AJ, Crawford KHD, Bloom JD. 2020. Attenuated influenza virions expressing the SARS-CoV-2 receptor-binding domain induce neutralizing antibodies in mice. Viruses 12:987. https://doi.org/10.3390/v12090987.

47. Zhu F, Zhuang C, Chu K, Zhang L, Zhao H, Huang S, Su Y, Lin H, Yang C, Jiang H, Zang X, Liu D, Pan H, Hu Y, Liu X, Chen Q, Song Q, Quan J, Huang Z, Zhong G, Chen J, Han J, Sun H, Cui L, Li J, Chen Y, Zhang T, Ye X, Li C, Wu T, Zhang J, Xia NS. 2022. Safety and immunogenicity of a live-attenuated influenza virus vector-based intranasal SARS-CoV-2 vaccine in adults: randomised, double-blind, placebo-controlled, phase 1 and 2 trials. Lancet Respir Med https://doi.org/10.1016/S2213-2600(22)00131-X.

48. Chen J, Wang P, Yuan L, Zhang L, Zhang L, Zhao H, Chen C, Wang X, Han J, Chen Y, Jia J, Lu Z, Hong J, Lu Z, Wang Q, Chen R, Qi R, Ma J, Zhou M, Yu H, Zhuang C, Liu X, Han Q, Wang G, Su Y, Yuan Q, Cheng T, Wu T, Ye X, Zhang T, Li C, Zhang J, Zhu H, Chen Y, Chen H, Xia N. 2022. A live attenuated virus-based intranasal COVID-19 vaccine provides rapid, prolonged, and broad protection against SARS-CoV-2. Sci Bull (Beijing) https://doi.org/10.1016/j.scib.2022.05.018.

49. Sun W, Liu Y, Amanat F, Gonzalez-Dominguez I, McCroskery S, Slamanig S, Coughlan L, Rosado V, Lemus N, Jangra S, Rathnasinghe R, Schotsaert M, Martinez JL, Sano K, Mena I, Innis BL, Wirachwong P, Thai DH, Oliveira RDN, Scharf R, Hjorth R, Raghunandan R, Krammer F, Garcia-Sastre A, Palese P. 2021. A Newcastle disease virus expressing a stabilized spike protein of SARS-CoV-2 induces protective immune responses. Nat Commun 12:6197. https://doi.org/10.1038/s41467-021-26499-y.

50. Mendonca SA, Lorincz R, Boucher P, Curiel DT. 2021. Adenoviral vector vaccine platforms in the SARS-CoV-2 pandemic. NPJ Vaccines 6:97. https://doi.org/10.1038/s41541-021-00356-x.

51. Frantz PN, Barinov A, Ruffie C, Combredet C, Najburg V, de Melo GD, Larrous F, Kergoat L, Teeravechyan S, Jongkaewwattana A, Billon-Denis E, Tournier JN, Prot M, Levillayer L, Conquet L, Montagutelli X, Tichit M, Hardy D, Fernandes P, Strick-Marchand H, Di Santo J, Simon-Loriere E, Bourhy H, Tangy F. 2021. A live measles-vectored COVID-19 vaccine induces strong immunity and protection from SARS-CoV-2 challenge in mice and hamsters. Nat Commun 12:6277. https://doi.org/10.1038/s41467-021-26506-2.

52. Lu MJ, Dravid P, Zhang YX, Trivedi S, Li AZ, Harder O, Mahesh KC, Chaiwatpongsakorn S, Zani A, Kenney A, Zeng C, Cai CX, Ye CJ, Liang XY, Shimamura M, Liu SL, Mejias A, Ramilo O, Boyaka PN, Qiu JM, Martinez-Sobrido L, Yount JS, Peeples ME, Kapoor A, Niewiesk S, Li JR. 2021. A safe and highly efficacious measles virus-based vaccine expressing SARS-CoV-2 stabilized prefusion spike. Proc Natl Acad Sci U S A 118:e20261531. https://doi.org/10.1073/pnas.2026153118.